

A climatic trigger for catastrophic Pleistocene–Holocene debris flows in the Eastern Andean Cordillera of Colombia

N. HOYOS,^{1,2,3*} O. MONSALVE,¹ G.W. BERGER,^{4,†} J. L. ANTINAO,^{4,8} H. GIRALDO,¹ C. SILVA,¹ G. OJEDA,⁵ G. BAYONA,¹ J. ESCOBAR^{3,6} and C. MONTES^{1,7}

¹Corporación Geológica ARES, Bogotá, Colombia

²Departamento de Historia y Ciencias Sociales, Universidad del Norte, Barranquilla, Colombia

³Smithsonian Tropical Research Institute, Balboa, Ancón, Republic of Panamá

⁴Desert Research Institute, Reno, NV, USA

⁵Subsuelo3D S.A.S, Bogotá, Colombia

⁶Departamento de Ingeniería Civil y Ambiental, Universidad del Norte, Barranquilla, Colombia

⁷Departamento de Geociencias, Universidad de los Andes, Bogotá, Colombia

⁸Centro Nacional de Investigación para la Gestión Integrada de Desastres Naturales (CIGIDEN), Chile

Received 22 September 2014; Revised 19 February 2015; Accepted 10 March 2015

ABSTRACT: The geomorphology and stratigraphy of massive debris flows on the Eastern Andean Cordillera, Colombia, indicate two distinct deposits can be recognized. The lower Chinauta deposit covers 14 km² and has a thickness of ~60 m, whereas the upper Fusagasugá deposit covers 20 km² and has a thickness of ~20 m. The lower Chinauta section consists of matrix-supported gravels, with isolated boulders and massive to moderately bedded structure and local inverse grading. The upper section displays sequences of inversely graded, clast-supported gravels, with boulders >2 m in axial length, capped by massive, matrix-supported fine gravels. The latter are dissected by coarse, channelized gravels. We interpret these facies as a series of debris and hyper-concentrated flows dissected by river channels. The Fusagasugá deposit is dominated by massive to inversely graded matrix-supported gravels with isolated boulders. Single-grain, optically stimulated luminescence dates of the sandy-silty matrix of debris and hyper-concentrated flows constrain the timing of deposition of the Chinauta debris flow deposits between 38.9 and 8.7 ka. We postulate that millennial-scale climate variability is responsible for causing these massive debris flows, through a combination of elevated temperatures and increased rainfall that triggered runoff and sediment transport. Copyright © 2015 John Wiley & Sons, Ltd.

KEYWORDS: Andes; Colombia; debris flows; optically stimulated luminescence.

Introduction

Mountainous regions are particularly susceptible to debris flows and mudflows triggered by intense or prolonged rainfall, earthquakes, volcanic eruptions and glacier melt. Climate can play a critical role in initiating debris flows through control of water transport capacity and sediment availability (Blair, 2001; Keefer *et al.*, 2003; Barnard *et al.*, 2006; Benn *et al.*, 2006; Jones *et al.*, 2014). The age and interpretation of the genesis of debris flow deposits are therefore informative about the climate and environmental conditions that prevailed when they were generated. This information, in turn, contributes to a better understanding of Quaternary landscape and climate change (Thomas and Thorp, 1995; Korup and Clague, 2009). However, there have been few studies of debris flows and associated deposits (e.g. alluvial fans) in the tropics (Nott *et al.*, 2001; Wesnousky *et al.*, 2012) compared with the abundant records from temperate, dry regions (e.g. Blair, 2001; Benn *et al.*, 2006; Lugon and Stoffel, 2010; Jones *et al.*, 2014).

The eastern Andes of Colombia display geological, topographic and climatic conditions favorable for generation of debris flows, including: (1) high relief and large accommodation space from tectonic uplift, (2) the presence of loose sediments from glacial deposits and (3) pronounced Quaternary climate fluctuations (e.g. Van der Hammen, 1974; Helmens *et al.*, 1997). Debris flow alluvial fans are

ubiquitous along intra-montane basins and in the eastern foothills of the Eastern Cordillera in Colombia. However, little work has been done on the stratigraphy and chronology of these deposits, which is needed to determine if there is a relationship between their formation and regional processes, such as tectonic activity or climate (Quigley *et al.*, 2007; Spelz *et al.*, 2008; Jones *et al.*, 2014).

We investigated massive intra-montane debris flows in the Eastern Cordillera of the Colombian Andes (Fig. 1). We determined their geomorphology and stratigraphy using digital elevation data, seismic refraction surveys, and sedimentological and stratigraphic field observations. Age estimates for the flows were obtained by optically stimulated luminescence (OSL) dating. Finally, we compared the above data with regional climatic records, to constrain the timing and potential controls on the formation of these deposits.

Regional Setting

The Colombian Andes comprise three mountain ranges, the Western, Central and Eastern Cordilleras (Fig. 1). The Eastern Cordillera formed as an extensional basin during the Mesozoic and became tectonically inverted, deformed and uplifted during the Cenozoic (Colletta *et al.*, 1990; Dengo and Covey, 1993). To the west, the Eastern Cordillera is bordered by the Magdalena Valley, and to the east, by the Llanos foreland basin. The study area is located on the western slopes of the Eastern Cordillera, with elevations ranging from ~280 m a.s.l. in the Magdalena Valley to ~4000 m a.s.l. in the cordilleran highlands. The central section of the study area includes a broad syncline formed in the Middle–Late Eocene Fusagasugá

*Correspondence: Natalia Hoyos, Departamento de Historia y Ciencias Sociales, as above

E-mail: nbotero@uninorte.edu.co

†Deceased.

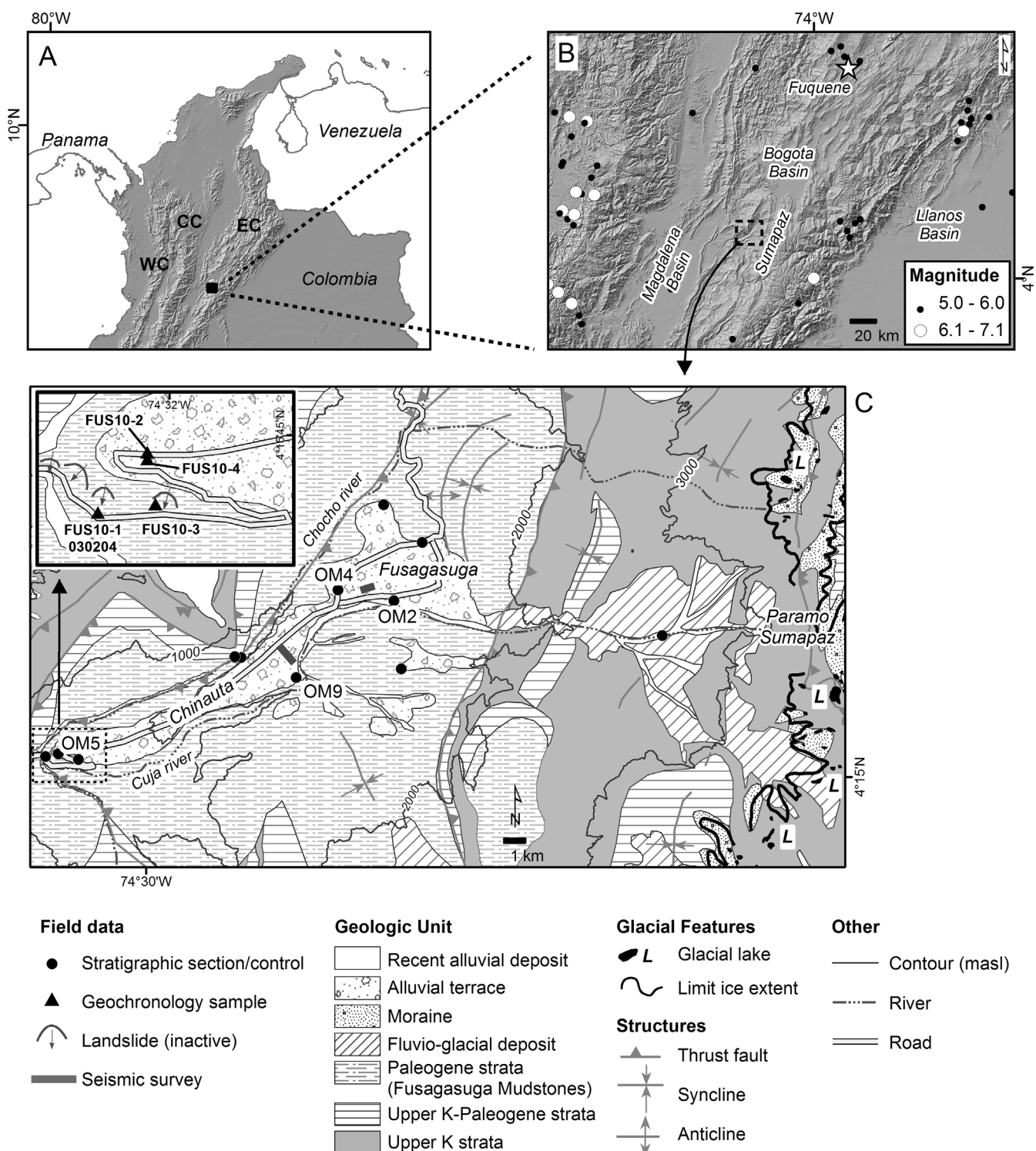


Figure 1. (A) Location of the study area showing the Western (WC), Central (CC) and Eastern (EC) cordilleras of the Colombian Andes. (B) Regional features of interest include the Magdalena Basin, Llanos Basin, Bogotá Basin, Sumapaz highlands and Lake Fuquene. Historical seismicity (1911–2014) is also shown for earthquakes of magnitude ≥ 5 (RSNC, 2014; USGS, 2014). (C) Simplified geologic map of the study area (modified from Acosta and Ulloa, 2001). Glacial lakes and limit of ice extent in Páramo de Sumapaz are from Helmens (1988). The Fusagasugá and Chinauta deposits are labeled as high alluvial terraces in existing geologic maps. Field data include stratigraphic sections and geochronology samples (inset). Only field stations mentioned in the text are labeled. Elevation data are from Shuttle Radar Topography Mission digital elevation model (USGS, 2006).

Mudstones, which consists of mudstones and siltstones, interbedded with feldspathic and lithic sandstones (Acosta and Ulloa, 1998; Bayona *et al.*, 2003) (Fig. 1). Debris flow deposits overlying the Fusagasugá Mudstones are described on geologic maps as Late Pleistocene ‘high alluvial terraces’ (Acosta and Ulloa, 2001). We avoid use of the latter term, however, because the stratigraphy and geochronology of

these deposits are poorly known. Two distinct debris flow deposits can be identified; the upper Fusagasugá deposit forms a fan with an apex at ~ 1600 m a.s.l., while the lower Chinauta deposit displays an elongated shape with a maximum elevation of ~ 1100 m a.s.l. The deposits are incised and drained by the Chocho River on the north-west and the Cuja River on the south-east (Fig. 1), both of which flow into the

Sumapaz River, a major tributary of the Magdalena River. In the highlands, east of the debris flow deposits, the cordilleran slopes are made of folded and faulted Paleogene and Cretaceous quartz sandstones, siltstones, mudstones and claystones (Acosta and Ulloa, 1998).

Paleoclimate records indicate that the Bogotá Basin (northeast of the study area, Fig. 1) was covered by a lake from late Pliocene to Pleistocene time (Van Geel and Van der Hammen, 1973; Van der Hammen, 1974; Hooghiemstra and Van der Hammen, 1993). There is also a record of several episodes of glaciation during the Pleistocene, with four moraine complexes identified in the Sumapaz highlands (Helmens, 1988; Fig. 1).

Methods

Geomorphic and seismic characterization

We used several morphometric indices to describe the geomorphology of the debris flow deposits. These indices were derived from a digital elevation model (90-m resolution; USGS, 2006) and included surface slope, aspect and terrain ruggedness. The last of these measures topographic heterogeneity and is based on the sum change in elevation between a grid cell and its eight neighbor grid cells (Riley *et al.*, 1999). We used these indices to determine the areal extent of the debris flow deposits. All calculations were performed in ArcGIS v10.

We also conducted geophysical studies to shed light on the subsurface geometry and thickness of these deposits. Two seismic refraction surveys were run, one on each of the Fusagasugá and Chinauta deposits. The Fusagasugá survey consisted of four adjacent seismic lines, totaling 624 m in length. Receivers were positioned every 6 m along the lines of section, with shot positions at both ends of each line as well as intermediate points, using a sledge hammer as the seismic source. The Chinauta survey consisted of a 930-m-long seismic line acquired with an array of 60 wireless sensors spaced every 15 m, using a tamping hammer as the seismic source.

Sedimentology

We studied nine field exposures (Fig. 1) that ranged in thickness from 2 to ~20 m, to characterize: (1) lithofacies, including lateral and vertical associations, continuity, internal sedimentary structures (e.g. grading, bedding, sorting), clast and matrix proportion and composition; (2) features that could be used as chronologic markers within the deposits, such as paleosols, erosional unconformities, changes in clast composition and facies associations; and (3) deposit thickness. Using data from these exposures, we created a

composite log that spans elevations from ~780 to 1450 m a.s.l. (Fig. 2). For our lithofacies characterization we used the terminology proposed by Miall (1996) for gravel lithofacies in fluvial and debris flow deposits. According to this system, a lithofacies code includes a first uppercase letter that refers to the dominant grain size (e.g. 'G' for gravel), and a second lower case letter for internal structure (e.g. 'm' for matrix-supported, 'c' for clast-supported). In our case, we used the term 'matrix' to refer to the dominant finer fraction. For most lithofacies, the matrix included sand, granule and pebble-sized grains, with little silt.

Geochronology

OSL ages were used to develop a temporal framework for the debris flow deposits. Potential confounding factors that can affect the reliability of OSL ages on these debris flow deposits include (1) limited exposure of sediment grains to daylight during transport and (2) the low luminescence sensitivity of quartz in tectonically active environments (Rittenour, 2008; Thrasher *et al.*, 2009; Lang, 2013 and references therein). Despite these potential drawbacks, we chose to use the OSL method because our deposits contain abundant quartz of sedimentary origin in the matrix, and organic remains that might be dated by radiocarbon methods are scarce. To overcome the first above-mentioned problem, application of OSL dating to the Fusagasugá and Chinauta deposits is based on the premise that a subset of grains were bleached (exposed to light) before the event, then carried by the flow and rapidly buried (cf. Chen *et al.*, 2008; Srivastava *et al.*, 2009). Under these conditions, discrimination of the best subset of mineral grains to be dated relies on single-grain techniques (Wu *et al.*, 2010) and elimination of unstable signals, as we indicate below. To assess the applicability of the technique to the matrix of debris flow deposits, we also tested the OSL response of sediments deposited by a sub-recent (1983) debris flow in western Nevada (Glancy and Bell, 2000), in a similar setting and lithology.

Samples for OSL dating were collected on the southwestern flank of the Chinauta deposit, where outcrops are exposed along a road that descends from the Chinauta Plain to the Sumapaz River (Figs 1 and 2; Table 1). Two samples were taken at the base of this section (FUS10-1, FUS10-3), and two were taken near the top (FUS10-4, FUS10-2). Samples were collected at night using low-intensity, filtered light-emitting diodes (Berger and Kratt, 2008), and placed in opaque plastic bags after removing ~2 cm of surface sediment. For our additional experiment in a sub-recent debris flow, we collected a sample from the distal fan created by the 1983 Slide Mountain debris flow near Reno, Nevada (Glancy and Bell, 2000), by extracting it through metal pipes inserted

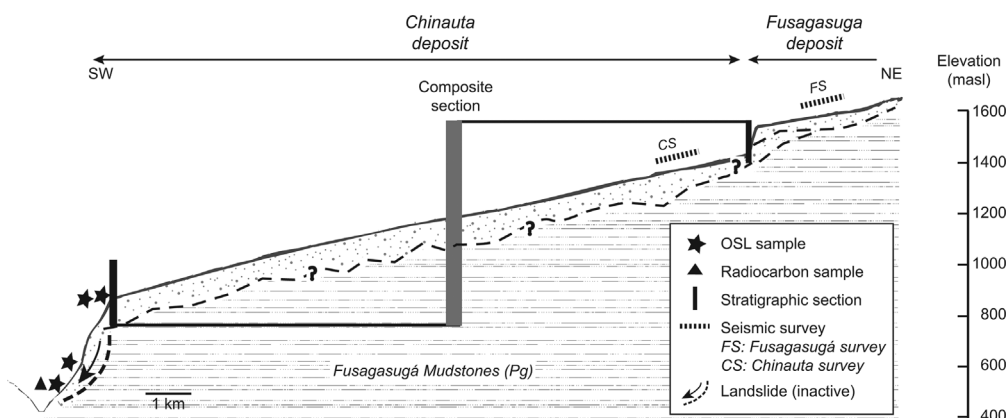


Figure 2. Schematic representation of the Fusagasugá and Chinauta deposits, showing our approach for the stratigraphic characterization, geochronological sampling and seismic data acquisition.

Table 1. Relevant characteristics of geochronology samples. Samples from the Chinauta deposit are listed from higher to lower elevation.

Sample	Latitude (°)	Longitude (°)	Elevation (m a.s.l.)	Analysis	Remarks
OPR10-1	39.2895	-119.8247	1540	Luminescence	Upper level, distal apron of 1983 Slide Mountain debris flow, eastern Sierra Nevada, USA
FUS10-2	4.2610	-74.5354	840	Luminescence	Upper level of Chinauta deposit, approximately 2 m from the surface
FUS10-4	4.2603	-74.5354	830	Luminescence	Upper level of Chinauta deposit, approximately 15 m from the surface
FUS10-3	4.2562	-74.5346	606	Luminescence	Colluvial deposits on the lower slopes of the Chinauta deposit, slid from middle to lower section of deposit
030204 and FUS10-1	4.2554	-74.5399	556	¹⁴ C, luminescence	Colluvial deposits on the lower slopes of the Chinauta deposit, slid from middle to lower section of deposit

in platforms on the walls of 1-m hand-excavated pits (OPR10-1). All samples were processed at the E.L. Cord Luminescence Laboratory of the Desert Research Institute. Fine-sand (62–225 µm, mostly 180–225 µm) quartz fractions were prepared as follows. Carbonates and organic matter were removed using 1 m HCl and 30% H₂O₂, respectively. Non-magnetic fractions were treated with 48% HF for 90 min to dissolve feldspars, followed by 20% HCl to dissolve precipitated fluorides (Aitken, 1998). The samples were tested for residual feldspar grains using a 40-s beta irradiation followed by observation of infrared luminescence. A portion of each sample was analysed for saturation water concentration, U and Th content using thick-source alpha-particle counting (Huntley and Wintle, 1981) and K content

using commercial atomic-absorption spectrophotometry to calculate the ionizing radiation dose rate to the OSL sample from the surrounding sediment (Aitken, 1998; Table 2). The luminescence age, in calendar years, is calculated as the paleodose (D_E) divided by the radiation dose rate (D_R) from the environment. D_E is a measure of the total radiation the sample has been exposed to since its last daylight exposure. We measured D_E values using a single-grain modified-SAR procedure (e.g. Berger *et al.*, 2013). A range of preheat and cutheats were used for the natural dose measurements (Table 3). Before each regeneration cycle, a blue light 'optical wash' was given to the grains for 40 s at a temperature 20 °C higher than the preheat temperature. Experiments were conducted with a single-grain Risø reader (model DA-20)

Table 2. Dose-rate data for luminescence age calculations. Samples are listed from higher to lower elevation.

Sample*	Water†	K ₂ O‡ (wt%)	$C_t\$$ (ks ⁻¹ cm ⁻²)	$C_{th}\$$ (ks ⁻¹ cm ⁻²)	$D_{CR}\$$ (Gy ka ⁻¹)	Dose rate** (Gy ka ⁻¹)
OPR10-1	0.08 ± 0.02	3.44	1.680 ± 0.013	0.684 ± 0.044	0.22 ± 0.02	5.68 ± 0.14
FUS10-2	0.15 ± 0.04	0.34	0.8008 ± 0.008	0.320 ± 0.026	0.16 ± 0.02	2.007 ± 0.088
FUS10-4	0.13 ± 0.03	0.76	0.7285 ± 0.0088	0.326 ± 0.029	0.03 ± 0.01	2.336 ± 0.081
FUS10-3	0.13 ± 0.03	1.26	1.1204 ± 0.011	0.644 ± 0.041	~0	2.77 ± 0.10
FUS10-1	0.15 ± 0.04	0.70	0.8718 ± 0.0090	0.439 ± 0.032	~0	2.045 ± 0.091

*The first row of data for each sample comprises data for sediment immediately surrounding the primary sample and are used to calculate the β contribution to the dose rate, while the second row represents data for samples taken 10–30 cm away from the primary sample, used to calculate the γ dose-rate component.

†Weight of water/weight of dry sample under burial conditions. Values were estimated from data for sediments at similar climatic settings, with constraints imposed by measuring present-day water content under current climatic conditions and saturation values for subsamples taken in the field (Table S1).

The potassium value for material around the quartz grains, with estimated uncertainty set to ± 0.05%. The internal K content is set to zero for dose-rate calculation of quartz separates. A small empirically estimated internal dose rate for typical quartz is added later (see **).

Total and thorium count rates from finely powdered samples for thick-source-alpha particle-counting (TSAC) method (Huntley and Wintle, 1981). $C_u = C_t - C_{th}$. These values are inserted directly into the age equations of Berger (1988) with the internal dose-rate components set to zero (see **).

‡Cosmic-ray component estimated from the algorithm of Prescott and Hutton (1994).

§Calculated with the conversion factors given by Adamiec and Aitken (1998) using the equations of Berger (1988). The attenuation of β radiation across the sand grain is accounted for using attenuation factors from Aitken (1985). An estimated small internal dose rate in quartz of 0.05 ± 0.03 Gy ka⁻¹ (Murray, personal communication to G. Berger, 2004) is added to the calculated dose rate.

Table 3. Luminescence and ¹⁴C age estimates. Samples are listed from higher to lower elevation. All luminescence experiments are single grain with early light subtraction (Ballarini *et al.*, 2007).

Sample	Size (µm)	Heating*	Yield†	$D_E\$\$$ (Gy)	Age§
OPR10-1	62–90	180/160	79/4500	0.44 ± 0.06	0.077 ± 0.011 ka
FUS10-2	125–150	220/200	61/3000	17.5 ± 3.5 (CAM)	8.7 ± 1.8 ka
FUS10-4	185–225	220/200	106/3400	89.9 ± 4.9	38.5 ± 2.5 ka
FUS10-3	125–150	230/190	39/2000	106.0 ± 8.3	38.3 ± 3.3 ka
FUS10-1	125–150	230/180	78/4000	79.6 ± 4.6	38.9 ± 2.8 ka
030204	n/a	n/a	n/a	n/a	17.98–17.54 k cal a BP

*Preheating temperature followed by cut-heating temperature (°C).

†Grains accepted/grains measured.

‡Unless noted otherwise, these are three-parameter MAM ages (Galbraith *et al.*, 1999), unlogged when near zero (OPR10-1), using the procedures of Arnold *et al.* (2009). A central age model was used on the lowest five D_E values in the distribution for sample FUS10-2.

§ D_E divided by the respective dose rate in Table 2.

using calibrated on-plate beta sources. We used the early light subtraction approach for data processing to minimize the effect of slow and medium components detected in trial runs in the luminescence signal of some of the measured quartz grains (e.g. Ballarini *et al.*, 2007). In this way, the signal in the 0.068–0.255-s interval was subtracted from the first 0.068 s of signal to calculate L/T (test dose-normalized luminescence signals) ratios. We accepted data having recycling ratios within 10% of unity at 1σ , recuperation values within 2σ of zero when recuperation was $>20\%$ of L_0/T_0 (L/T ratio for cycle $i=0$), and maximum test dose errors of 30%. We included a 12% internal (instrumentation) random error based on the systematic single-grain reproducibility tests of Thomsen *et al.* (2007).

For each sample, we plotted the D_E distribution obtained by applying the criteria above, using an inverse variance-weighted frequency density plot (Berger, 2010). For this plot, weighting is calculated using the inverse variance of the relative errors, not the inverse variance of the absolute errors. D_E distribution plots obtained from our analyses were used as a visual aid to recognize the presence and range of any cluster of ‘youngest-age’ D_E values, and to select a method for the calculation of the D_E value used in the estimation of a burial age. After visual inspection of D_E histograms, we analysed distributions using

either an error-weighted mean of specific subsets or through a Central Age (CAM) or Minimum Age Model (MAM) (three- or four-parameter) (Galbraith *et al.*, 1999; Arnold *et al.*, 2009). Calculated ages are given in Table 3. To check the OSL ages, we searched the sections for organic remains to date by radiocarbon. We found only one sample consisting of carbonized root material, which came from the lower portion of the road section where one of the OSL samples was taken. The sample was submitted for accelerator mass spectrometry dating to Beta Analytic (Miami, FL, USA). The radiocarbon age was calibrated using the program Oxcal-Intcal13 (Bronk-Ramsey, 2001, 2008; Reimer *et al.*, 2013).

Results

Geomorphic and seismic characterization

Two relatively flat surfaces, clearly different from the surrounding rugged topography, can be differentiated based on their surface slope and terrain ruggedness (Fig. 1). The upper surface, associated with the Fusagasugá deposit, exhibits a fan shape with a long axis that runs ESE–WNW for ~ 7 km. It is a west-facing, smooth surface, with an average slope of 5°, an extent of 19.8 km^2 , maximum width of 5.3 km and an elevation range from 1800 m a.s.l. at the apex to

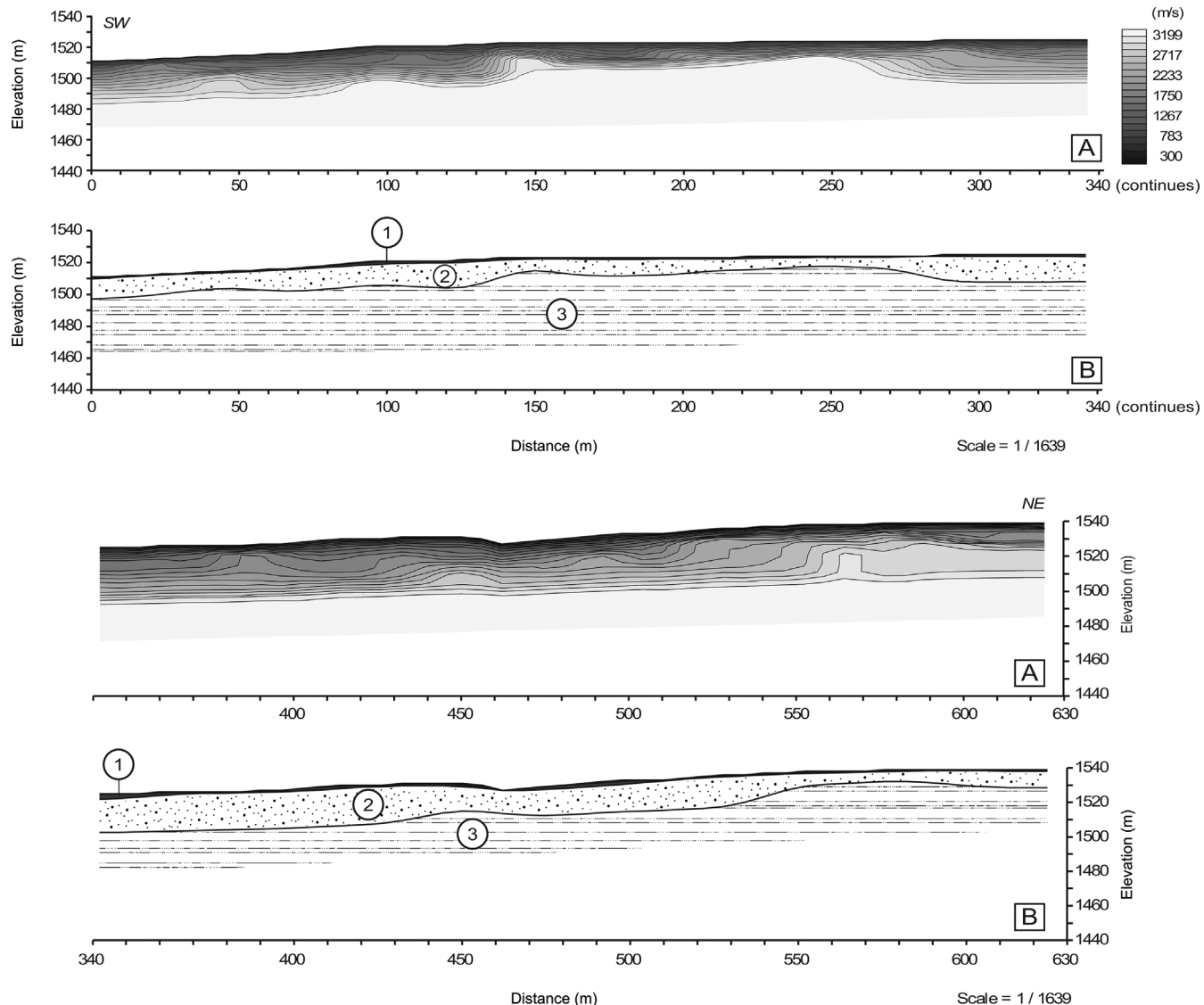


Figure 3. (A) Seismic data and (B) interpretation of the Fusagasuga deposit seismic survey (630 m length). Layers include (1) compacted soil, (2) water-saturated sedimentary layer and (3) Cenozoic basement. The uppermost layer, interpreted as non-compacted soil, is not visible at this scale. Note the irregular geometry of the interface between the upper layers and the basement. For location of profile refer to Figs 1 and 2.

1420 m a.s.l. at the most distal margin. The lower surface is associated with the Chinauta deposit, and is located southwest of the Fusagasugá deposit. It does not have a typical fan shape; it is elongated in the NE-SW direction and its long axis is 14 km in length. This deposit faces south-west and is relatively flat (average slope of 6°), with a smooth surface and steep flanks that descend abruptly to the northwest and south-east. The surface area of the Chinauta deposit is 14.4 km² and it has a maximum width of 2 km. Elevations range from 1370 m a.s.l. in the proximal area (NE) to 840 m a.s.l. on the south-western flank.

The Fusagasugá seismic refraction survey revealed three shallow layers with P-wave velocities of 300, 700 and 1500 m s⁻¹, overlying a layer with a P-wave velocity of ~3000 m s⁻¹. The three shallow layers are interpreted as non-compacted soil, compacted soil and a water-saturated sedimentary layer, respectively (Fig. 3). The deepest layer is interpreted as the Cenozoic ‘basement’. The three shallow layers are bounded by non-planar, irregular surfaces. Thickness varies laterally, and ranges from <10 m at the edges to ~30 m at the center. The maximum thickness is consistent with our stratigraphic characterization, which yields a maximum thickness of the Fusagasugá deposit of ~15–20 m (Fig. 4).

The seismic refraction survey of the Chinauta deposit reveals a single top layer with a P-wave velocity of 1030 m s⁻¹ overlying the 3000 m s⁻¹ basement. In contrast to the Fusagasugá deposit, no internal geometry was resolved above the basement. The thickness of the top layer ranges from ~28 to ~50 m. The top layer is interpreted to be the bulk of the Chinauta deposit; it rests unconformably on a Cenozoic basement similar in acoustic character to the basement imaged under the Fusagasugá deposit. Our stratigraphic observations indicate that the maximum thickness of the Chinauta deposit is ~55–60 m. The irregular paleotopography buried below the Fusagasugá and Chinauta deposits precludes a precise estimation of their total volume.

Sedimentology

A composite log of the Fusagasugá and Chinauta deposits is shown in Fig. 4, and details for each facies are presented in Table 4. Exposures of the Fusagasugá deposit are dominated by facies Gm2, which here consists mainly of cobble- to boulder-sized clasts with axial lengths reaching 1–2 m (Fig. 4). Locally, this facies is clast-supported. The matrix is mostly sandy, and clasts are typically subangular to subrounded and consist of quartz and lithic sandstones, purple mudstones, gray shale and chert. Elongated clasts are not preferentially aligned. Structure is massive to inversely graded. Bed thickness is between 2 and 4 m and beds are laterally continuous. Bed boundaries are not sharp, but can be recognized by changes in clast size, specifically the presence or absence of large boulders. The lower part of this deposit was observed only at one field station (OM4) (Figs 4 and 5).

The upper ~15 m of the Chinauta deposit consists of, from top to bottom, Gm1, Gm2 and Gc (Figs 4–6). This sequence is identifiable at proximal and distal ends of the Chinauta deposit. Facies Gm1 consists of massive, matrix-supported granule to fine pebble-sized gravels, within a predominantly sandy to silty matrix. Average bed thickness is 1–2 m, but is highly variable. This facies is easily discernible because of its massive structure, matrix and relatively small clast size. Facies Gm2 consists of cobble- and boulder-sized clasts embedded in a matrix of sand, granule and pebble-sized grains. Clast content ranges from 20 to 40%. Boulders can reach 1.5 m in axial length. Structure is mostly inversely

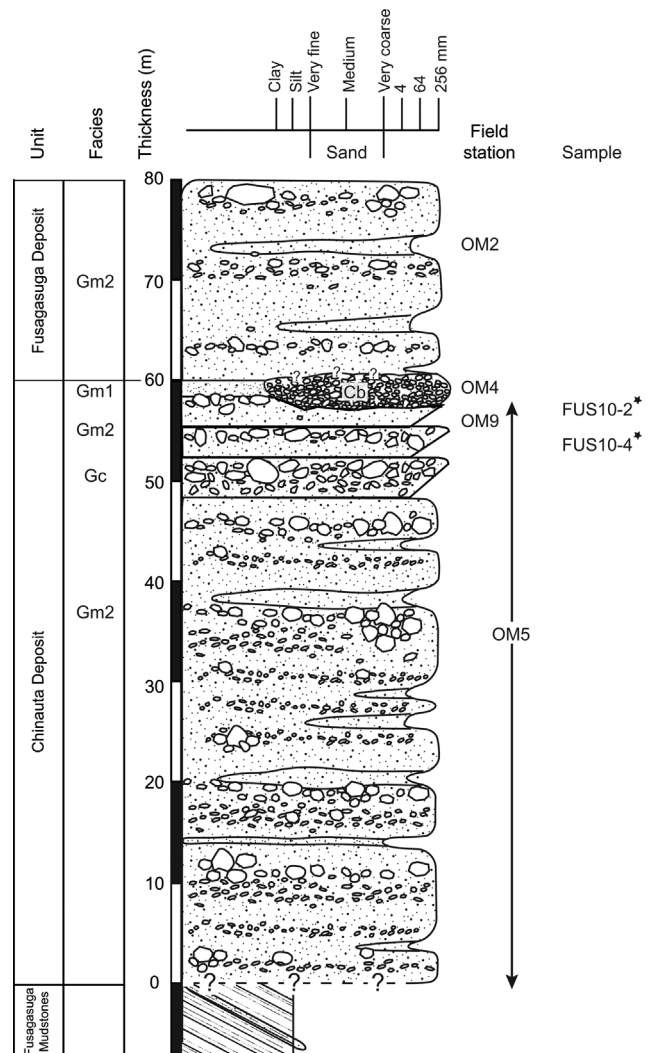


Figure 4. Composite log for Fusagasuga and Chinauta deposits, including field stations and geochronology samples. Grain size represented refers to dominant grain size for fraction <256 mm. Samples FUS10-1 and FUS10-3 are not shown as they were collected on sections suspected to be affected by mass wasting.

graded. Individual beds are 2–3 m, with the tops defined by the presence of large boulders (Fig. 6). Gm2 overlies facies Gc, a clast-supported, granule- to boulder-sized gravel, easily recognized by its greater boulder content (>50% of the clasts) and size (locally >2 m in axial length). Facies Gc also exhibits inverse grading, with individual beds 2–3 m thick, and local lensing. Clast composition in the above facies sequence includes quartz and lithic sandstones, purple mudstones, gray shale and chert. No preferred alignment of elongated clasts was observed. The top of this sequence is locally unconformably overlain by facies Cb, which consists of medium- to well-sorted, clast-supported gravels with some imbrication and sharp, channel-shaped boundaries (Figs 5 and 6).

The lower part of the Chinauta deposit is dominated by facies Gm2 with texture similar to the one described for the upper Chinauta section. Facies structure in this lower level is massive to bedded, with local lensing and inverse grading. The presence of isolated pockets of angular to subangular boulders with axial lengths up to 1.5 m is noticeable (Fig. 7). Lenses are ~0.2–0.5 m thick and consist of granule- to cobble-sized gravels embedded in a sandy matrix. Individual beds are 1.5–3.0 m thick, with the tops defined by the largest clast levels within the inversely graded sequence. Clasts are

Table 4. Fusagasugá and Chinauta deposits facies descriptions and interpreted depositional process. Distinctive features of each facies are highlighted in bold italic. Depositional processes interpretation from Pierson and Costa (1987) Scott (1988) Miall (1996) Sohn *et al.* (1999; Blair (2001) and Pierson (2005).

Facies	Description	Depositional process
Gm1 Massive matrix-supported fine gravel	Unsorted mixture of granules and fine pebbles with few isolated boulders, which are supported in a finer fraction (matrix-supported). Matrix is sandy to silty. Clasts are mostly subangular to subrounded. Structure is massive, although there is some local normal grading.	Hyper-concentrated flow
Gm2 Matrix-supported gravels, massive to inversely graded, with local bouldery levels and incipient to moderate bedding.	Unsorted mixture of cobbles and boulders, subangular to subrounded, which are supported in a finer fraction (matrix-supported). Largest clasts reach diameters ~200 cm. Matrix is made of sand, granule and pebble-sized grains. Locally, this facies can be clast-supported. Structure varies from massive to incipient/well-developed inversely graded and can also exhibit lenticular structures and incipient to moderate bedding .	Transitional between debris flow and hyper-concentrated flow
Gc Bouldery, clast-supported gravel with inverse grading	Mixture of granules, pebbles, cobbles and boulders, subangular to subrounded. Largest clasts reach diameters ~200 cm. This facies is mostly clast-supported , but can be locally matrix-supported, and exhibits well-developed inverse grading . Matrix is made of sand, granule and pebble-sized grains.	Debris flow
Cb Coarse gravel in channels	Moderately to well-sorted , clast-supported coarse pebble- to small boulder-sized gravel, showing incipient to moderate imbrication . Clasts are angular to subrounded. Beds are discontinuous in transverse cuts, exhibit lensing and rest on sharp, channel-shaped surfaces.	Bedload deposition within high-energy channels

quartz and lithic sandstones, purple mudstones, gray shale and chert. Shale is particularly abundant in the lowest part of the Chinauta deposit. This facies unconformably overlies the Fusagasugá Mudstones.

Geochronology

OSL and radiocarbon results are presented in Tables 2 and 3. Additional data are presented in the Supporting Information (Table S1, Fig. S1). Results for burial doses obtained from sample OPR10-1 in a sub-recent (1983) debris flow are encouraging (Fig. 8). First, the overestimation of the age (77 ± 11 years compared with 27 years, i.e. ~50 years) is similar or smaller than that found in flash flood, alluvial and fluvial systems (30–300 years; e.g. Murray *et al.*, 2012; Medialdea *et al.*, 2014; Brown *et al.*, 2015) where the mechanism for deposition allowed more bleaching time than the short time expected in a debris flow. Second, the overestimation (~50 years) is negligible when compared with the uncertainty (1800–3300 years) in the age estimates for the FUS samples. Although the assumption of previous bleaching needs further testing with debris flows of different ages and

physical properties, these two results do not contradict our initial assumption, and provide further support to the idea that sandy–muddy matrix debris flows can be dated with single-grain OSL methods. For the OPR10-1 sample we also tested the difference between ages calculated with an unlogged (Arnold *et al.*, 2009) MAM model in a population including D_E negative values (0.52 ± 0.04 Gy), and ages calculated with the logged MAM model but excluding those values (0.44 ± 0.06 Gy). We found no statistical difference between them, and therefore we chose to use the more robust logged MAM model for all the FUS samples.

Dose recovery tests (Fig. S1) in FUS samples indicate that the SAR method can be used in this setting, with the caveat of low sensitivity (hence larger uncertainties in measurements, e.g. Fig. 9, and a low proportion of usable grains, see Table 3). There is indeed a notable similarity between OPR and FUS samples in this regard, with yields ranging between 1 and 3% of usable measured grains.

All D_E distributions for FUS samples appear positively skewed (Fig. 9), indicating that simple averages or CAM ages are not a good representation of the true burial dose needed to calculate an age. Taking this into account, calculated OSL

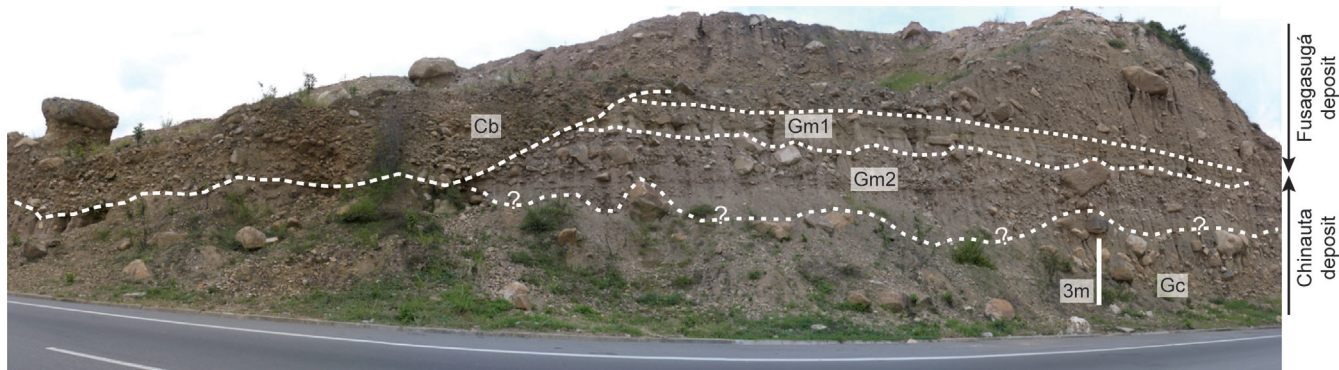


Figure 5. Contact between the Fusagasugá and Chinauta deposits along the highway west of Fusagasugá. Question marks at the upper boundary of facies Gc indicate sections concealed by debris. Base of section is at 1404 m a.s.l. For location see field station OM4 in Fig. 1. (Photo credit: O. Monsalve.) This figure is available in colour online at wileyonlinelibrary.com.

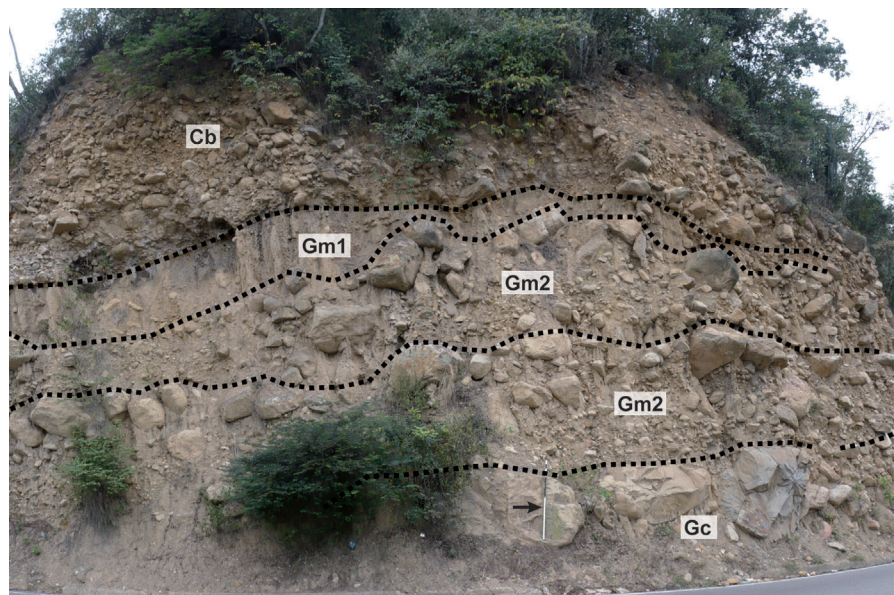


Figure 6. Upper section of the Chinauta deposit showing the following facies sequence from top to bottom: Gm1, Gm2 and Gc. The top of this sequence is dissected by facies Cb. Arrow points at 1.5-m scale. Base of section is at 798 m a.s.l. For location see field station OM5 in Fig. 1. (Photo credit: O. Monsalve.) This figure is available in colour online at wileyonlinelibrary.com.

ages range between 8.7 ± 1.8 ka for the uppermost sample (FUS10-2, 840 m a.s.l.) to 38.9 ± 2.8 ka for the lowermost sample (FUS10-1, 556 m a.s.l.). Intermediate samples at 830 m a.s.l. (FUS10-4) and 606 m a.s.l. (FUS10-3) yielded OSL ages of 38.5 ± 2.5 and 38.3 ± 3.3 ka, respectively. The radiocarbon sample (030204) yielded a calibrated age of 17.98–17.54 cal ka BP (Table 3). The discrepancy between the OSL and radiocarbon ages is addressed below.

Discussion

Depositional processes

The Fusagasugá and Chinauta deposits exhibit geomorphic and stratigraphic features characteristic of debris flows, such as a relatively flat surface, massive or inversely graded structure, a poorly sorted clast fraction, little or no preferential clast alignment, mixed subangular and angular clasts, presence of large boulders, and large vertical and lateral variability (Scott, 1988; Miall, 1996; Major, 1997; Sohn *et al.*, 1999; Blair, 2001; Benn *et al.*, 2006; Srivastava *et al.*, 2009). The geomorphic, seismic and stratigraphic characteristics

indicate that at least two distinct major depositional events occurred. The first event led to formation of the Chinauta deposit, and the second was responsible for the Fusagasugá deposit. These two events are differentiated by (1) geomorphology, with differing direction and shape, and (2) stratigraphy, with facies Cb marking the end of deposition of the Chinauta deposit. Within each deposit there is no clear stratigraphic evidence (i.e. paleosols, post-depositional fluvial channels) for the occurrence of multiple, temporally separate events. Experimental work on debris flow deposits, however, shows that multiple events cannot be ruled out simply based on stratigraphy as temporally distinct events yield massive deposits with little stratigraphic marker horizons (Major, 1997).

The geochronology results suggest that the Chinauta deposit records at least two events (Table 3). We therefore hypothesize that the Chinauta deposit accumulated by incremental aggradation because of multiple pulses or events, as reported for other debris flow deposits (Sohn *et al.*, 1999; Cui *et al.*, 2005). Features of the Chinauta deposit that favor multiple aggradation events include (1) the presence of several inversely graded sequences and facies interpreted as transitional between debris and hyper-concentrated flows (Gm2), and (2) large differences in facies between the lower and upper levels. For instance, lensing and bedding are frequent in the lower levels of this deposit, whereas the upper levels show clear inverse grading and have more and larger clasts that form continuous beds. One explanation for inverse grading in distal areas of debris flow deposits is that coarse clasts move up and away from the lower boundary due to inter-particle interactions (Major, 1997). Inverse grading can also result from the transformation of debris to hyper-concentrated flow, as the leading edges of the debris flow mix with streamflow. The resultant deposits will include hyper-concentrated flow deposits overlaid by debris flow deposits (Pierson and Scott, 1985). By contrast, we observed more and larger clasts in the distal area of the Chinauta deposit, consistent with longitudinal sorting as observed in other debris flows (Cui *et al.*, 2005; Hung, 2005).

We infer that the Chinauta deposit resulted from the following sequence of pulses or temporally distinct events. First, events that were transitional between debris and hyper-concentrated flows deposited the lower section, with sandier lenses representing channels that formed during the flow-waning phases (Srivastava *et al.*, 2009). Such variability in



Figure 7. Lower section of the Chinauta deposit, showing facies Gm2. The matrix in this section is mostly composed of sands, granules and pebbles. Base of section is at 795 m a.s.l. (Photo credit: N. Hoyos.) This figure is available in colour online at wileyonlinelibrary.com.

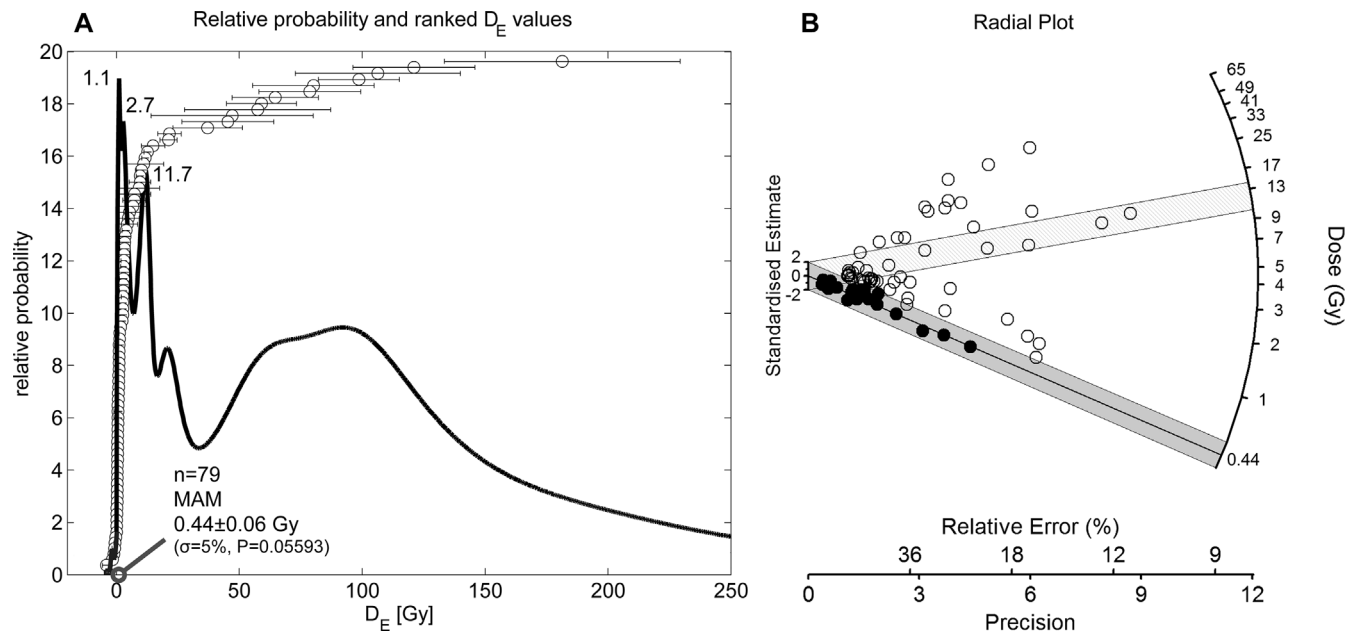


Figure 8. OSL results for sample OPR10-1. (A) Relative probability (transformed distribution) plot (e.g. Berger, 2010), and ranked values for D_E observations. This curve was obtained by weighing the contribution of each added value using its inverse variance. The minimum age model (Galbraith *et al.*, 1999) is displayed by a shaded circle on the x-axis. Overdispersion value used is 5%. Note peaks at 1.1, 2.7 and 11.7 Gy, and the presence of a few negative values in the lower spectrum of D_E values. (B) Radial plot. These plots (e.g. Galbraith *et al.*, 1999) are utilized when simultaneous visualization of a measurement's value and its precision is needed. Note the secondary well-defined peak at 11.7 Gy, as in A.

sediment concentration and flow viscosity within a single event has been reported elsewhere (Pierson and Scott, 1985; Sohn *et al.*, 1999; Dasgupta, 2003; Cui *et al.*, 2005). The upper Chinauta section was later deposited by debris flows with higher clast content and enough energy to mobilize the large boulders found in facies Gc. Subsequent hyper-concentrated flows deposited facies Gm1, probably during the late stage of the debris flow. The Chinauta deposit was later affected by surface erosion, which formed the local channel fills represented by facies Cb.

The Fusagasugá deposit also seems to have been formed by multiple surges from either a single event or several events, as indicated by the stacked, inversely graded levels. Exposed sections of this deposit, however, do not exhibit the large vertical variability, or distinctive, well-developed inverse grading seen in the upper levels of the Chinauta deposit. We could not assess longitudinal variability within the Fusagasugá deposit because of the lack of exposures in the proximal area. The larger runout distance and thickness of the Chinauta deposit points to an originating mechanism with higher erosion and transport energy relative to the Fusagasugá deposit (Rickenmann, 2005).

Given the geologic setting and geomorphologic characteristics of the studied deposits, glacial material on the eastern highlands (Sumapaz) is the most likely source of the sediments (Fig. 1). Five glacial sequences have been identified in this area, with ages ranging from >38 to 12.5 ka. Maximum ice extent occurred during the two oldest glaciations (>38 and 36–31 ka) when the ice front reached ~3000 m a.s.l. (Helmens *et al.*, 1997).

A large volume of material in the Fusagasugá and Chinauta debris flows is supported by the stratigraphic and seismic refraction data, which indicate thicknesses of up to 30 m in the Fusagasugá deposit and ~50 m in the Chinauta deposit. Assuming a conservative mean thickness of 10 m yields a total volume of 10^8 m 3 . We compared our volume estimates with values derived from large single-event debris flows ($\geq 10^5$ m 3). These include debris flows from Mount St Helens,

USA (10^6 – 10^8 m 3 : Major *et al.*, 2005 and references therein), the north-central Venezuelan coast (0.4 – 2.6×10^6 m 3 : Garcá-Martínez and López, 2005), Indonesia (1 – 5×10^5 m 3 : Lavigne and Suwa, 2004), Huascarán, Peru (4×10^7 m 3 : Lliboutry, 1975), Ruiz Volcano, Colombia (4.8×10^7 m 3 : Lowe *et al.*, 1986), and British Columbia, Canada (48.5×10^6 m 3 : Guthrie *et al.*, 2012). The largest of these reported debris flows originate in volcanic regions, e.g. Mount St Helens, Indonesia and Colombia, which is not the case for our deposits, even though they are estimated to be of equal or even greater volume.

Geochronology

Alluvial terraces and debris and hyper-concentrated flow deposits contained in them have been successfully dated by OSL techniques, despite the short resetting times (Suresh *et al.*, 2002; Chen *et al.*, 2008; Srivastava *et al.*, 2009; Ray and Srivastava, 2010; Zhang *et al.*, 2010). This suggests that bleaching before deposition may play a larger role for signal reset before transport and burial, as hypothesized by, for example, Medialdea *et al.* (2014) and as we also hypothesized in this study. The use of the silty–sandy fraction of the matrix as sample material, however, is an unusual approach, compared with the sands commonly targeted when dealing with debris flows (e.g. Chen *et al.*, 2008; Zhang *et al.*, 2010). Differences between OSL and radiocarbon results in this study were, however, a cause for concern. Nevertheless, three of the OSL samples returned consistent ages (~39–38 ka) for the Chinauta deposit, suggesting an unaccounted error associated with the radiocarbon age. After initial sampling and processing of all OSL samples, and during subsequent field visits, we found evidence for mass wasting on the lower slopes of the Chinauta deposit, and we suspect that material sampled for dating in the lower part of the section (FUS10-1, FUS10-3, 030204) may have come from a sliver of the deposit that was transported from above through rotational landsliding (Fig. 2). This hypothesis is

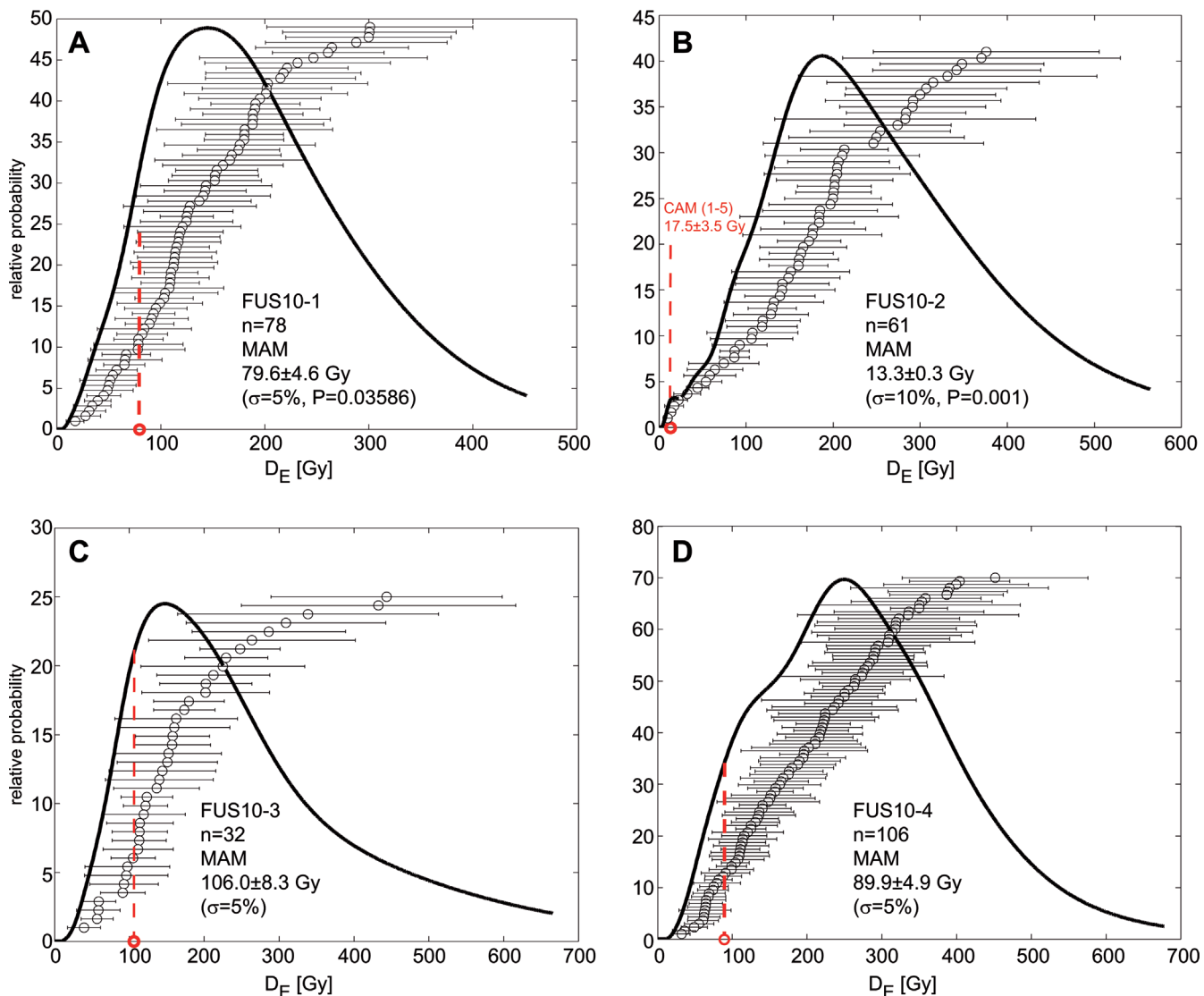


Figure 9. Relative probability (transformed distribution) plots for FUS samples, with ranked values for D_E observations. The MAM D_E (Galbraith *et al.*, 1999) value is indicated by vertical dashed line and open circles on the x-axis. (A) Sample FUS10-1. (B) Sample FUS10-2. MAM D_E is indicated but it was not used in the final age determination because the P model value was too small, indicating that the obtained MAM value is not representative of the lower end values in the distribution. Overdispersion value used in the MAM calculations is 10%. The vertical dashed line indicates a CAM (e.g. Galbraith *et al.*, 1999) calculated using the lower five values (grains 1–5). The same value can be obtained when the relative-error-weighted mean (REWm) plus associated error is calculated (Berger, 2010). The value of 17.5 ± 3.5 Gy obtained here also agrees with the lowest value obtained through a finite mixture model analysis (Galbraith and Green, 1990) with three subsets (Fig. 10). (C) Sample FUS10-3. Note MAM D_E value. (D) Sample FUS10-4. Note MAM D_E value. This figure is available in colour online at wileyonlinelibrary.com.

supported by: (1) field and seismic data indicating that the deposit–basement boundary is located at elevations higher than the lower samples, (2) the presence of thick wedges of colluvial material against the western flank of the Chinauta deposit (Fig. 1, also see Fig. S2) and (3) the fact that the two lower OSL sample ages [FUS10-1 (38.9 ka), FUS10-3 (38.3 ka)] are similar to the age of the higher sample FUS10-4 (38.5 ka). Because moderate bedding is still present at the lower sampling sites, landsliding was probably accomplished in a rotational manner, without disturbing the sequence and therefore without mixing and exposing the sediments to light, which is consistent with the similarities between upper and lower OSL ages and with field observations. The younger radiocarbon age on a rootlet might come from vegetation that grew on the deposit surface after it was laid down and possibly after being mobilized by mass wasting. Therefore, even though the lower sampled material may have moved, together the three lower Chinauta OSL samples (FUS10-1, 10-3 and 10-4) point to an early depositional event or series of events close to

38 ka. The age on the uppermost OSL sample from the Chinauta deposit suggests a more recent event at 8.7 ka. The Fusagasugá deposit would be younger than 8.7 ka.

Paleoclimate linkages

Common triggering mechanisms for debris flows include earthquakes (Blair, 2001; Schuster *et al.*, 2002; Keefer *et al.*, 2003; Benn *et al.*, 2006) and volcanic eruptions. The latter are absent during the Quaternary in this section of the Colombian Andes. Regarding the former, no large-magnitude earthquakes during the past ~100 years have been recorded for the Eastern Cordillera (Fig. 1). Based on these observations and on the large volume of the Fusagasugá and Chinauta deposits, we suggest that extreme climate events are a more likely cause of the multiple debris and hyper-concentrated flows documented in our study. The OSL-based chronology therefore provides a time framework for inferring possible causal mechanisms for the debris flows linked to paleoclimate records.

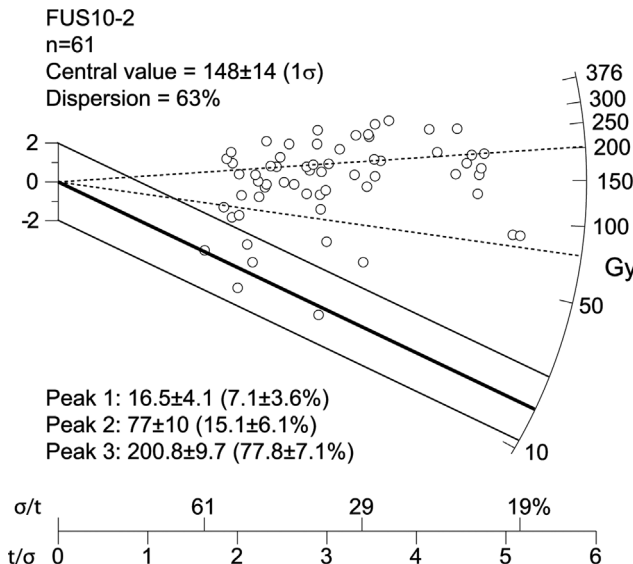


Figure 10. Radial plot for sample FUS10-2; same dataset as in Fig. 9B. A finite mixture model (Galbraith and Green, 1990) is shown, separating the whole population into three discrete resolvable populations, each one identified by a certain 'peak' value. Note that the lowermost peak (16.5 ± 4.1 Gy) is similar to the CAM value obtained for the lowest five data points (Fig. 9B). RadialPlotter software was used to prepare the diagram (Vermeesch, 2009).

Paleoclimate records and glacial geomorphology studies indicate high climate variability for this region throughout the Pleistocene and Holocene, with a series of alternating stadials and interstadials up to the Holocene interglacial (Helmens, 1988; Van der Hammen, 1995; Groot et al., 2011). The OSL age of $\sim 38 \pm 3$ ka for the deposits is close to the timing of Greenland interstadial 8 (Grootes et al., 1993), and marks the Tenjo interstadial in the Colombian Andes (Van der Hammen, 1995). The high-resolution Fuquene pollen record from the Bogotá Basin (Fig. 1) indicates a remarkable increase in mean annual temperature of 4°C at 2540 m asl from ~ 40 to ~ 36 k cal a BP (Groot et al., 2011). A large amount of meltwater might have been caused by this temperature increase. Furthermore, the same record indicates an increase in deep water vegetation and high lake level fluctuations during interstadial 8 (Groot et al., 2013) that we interpret as a period of possible higher precipitation. This increase in temperature and precipitation happened right after the end of Heinrich stadial H4 (Hemming, 2004), which has been documented as a cold and dry period in northern South America (Helmens et al., 1997; Peterson et al., 2000) and Central America (Hodell et al., 2008; Escobar et al., 2012). A simultaneous southward displacement of the Intertropical Convergence Zone (ITCZ) during H4 has been documented by an increase in precipitation in otherwise semi-arid north-eastern Brazil (Wang et al., 2004–2007). A more northward position of the ITCZ after H4, together with an increase in mean annual temperatures and precipitation (Groot et al., 2011–2013), might have enhanced runoff and sediment transport in this section of the Colombian Andes generating the thick lower section of the Chinauta deposit.

By the early Holocene, a period of higher precipitation, relative to present-day values, is documented by the Fuquene diatom record, which displays the highest water levels since the Last Glacial Maximum from ~ 9.6 to 7.9 k cal a BP (Velez et al., 2003). Rapidly increasing temperatures (e.g. Groot et al., 2011) combined with enhanced rainfall, generated conditions for enhanced runoff and higher potential for debris-flow triggering. This favored the formation of the upper Chinauta deposit. It is also likely that changes in precipitation

patterns caused by a northward movement of the ITCZ during the early Holocene (Haug et al., 2001) contributed to the generation of the upper Chinauta section. The paleoclimate arrangement of the lower dated section is consistent with that of the upper section, i.e. the combination of increasing temperatures (Groot et al., 2011) and movement of the ITCZ into a northern position in South America (Haug et al., 2001; Wang et al., 2007). We therefore consider that the climatic triggering hypothesis is robust, compared with seismic or volcanic triggers.

Conclusions

We have documented massive debris flow deposits in the Eastern Andean Cordillera of Colombia, by successfully applying single-grain OSL dating to the sandy-silty matrix of debris and hyper-concentrated flows. The geomorphic characterization of the observed deposits suggests that they consist of two separate sequences, the Fusagasugá and Chinauta deposits. Interpretation of the stratigraphy indicates that these deposits formed by multiple pulses, transitioning between debris and hyper-concentrated flows. Large-magnitude debris flows formed the bulk of the Chinauta deposit between ~ 39 and 38 ka. The uppermost level in this deposit formed ~ 9 ka. Both periods were marked by large regional climate variability that consistently points to a sharp increase in rainfall and enhanced meltwater discharge caused by higher temperatures. These deposits provide an important record of the geomorphic response of tropical mountain systems in northern South America to climate and environmental change during the late Pleistocene and early Holocene. Dating of similar deposits on the eastern slopes of the Eastern Cordillera is warranted to assess the regional extent of these processes.

Supporting Information

Additional supporting information may be found in the online version of this article at the publisher's web-site.

Table S1: Measured, present-day water content for sampling sites, and water content for the same sediment, when saturated.

Figure S1: Dose recovery test results.

Figure S2: View of the south-western margin of the Chinauta deposit.

Acknowledgements. N.H. was supported by grants from Fundación para la Promoción de la Investigación y la Tecnología del Banco de la República (grant 2655), Colciencias (Fondo para la Ciencia, la Tecnología y la Innovación) and Universidad del Norte (internal research grant). Collection and processing of OSL samples was made possible by a US National Science Foundation (NSF) grant (1015665) to G.W.B., and H.G. was supported by Colciencias (Fondo para la Ciencia, la Tecnología y la Innovación). We thank Paul Verburg for his support in retrieving OSL data. We also thank Mark Brenner, John Clague, Sophie Baker and an anonymous reviewer for their careful revision of this manuscript.

Abbreviations. CAM, Central Age Model; ITCZ, Intertropical Convergence Zone; MAM, Minimum Age Model; OSL, optically stimulated luminescence.

References

- Acosta JE, Ulloa CE. 1998. *Geología de la Plancha 246 Fusagasugá*. Ingeominas: Bogotá.

- Acosta JE, Ulloa CE. 2001. Memoria explicativa. Geología de la Plancha 246 Fusagasugá, escala 1:100.000. Ingeominas: Bogotá.
- Adamiec G, Aitken MJ. 1998. Dose-rate conversion factors: update. *Ancient TL* **16**: 37–50.
- Aitken MJ. 1985. *Thermoluminescence dating*. Academic Press: San Diego.
- Aitken MJ. 1998. *An Introduction to Optical Dating: the Dating of Quaternary Sediments by the Use of Photon-Stimulated Luminescence*. Oxford University Press: Oxford.
- Arnold LJ, Roberts RG, Galbraith RF et al. 2009. A revised burial dose estimation procedure for optical dating of young and modern-age sediments. *Quaternary Geochronology* **4**: 306–325.
- Ballarini M, Wallinga J, Wintle AG et al. 2007. A modified SAR protocol for optical dating of individual grains from young quartz samples. *Radiation Measurements* **42**: 360–369.
- Barnard PL, Owen LA, Finkel RC. 2006. Quaternary fans and terraces in the Khumbu Himal south of Mount Everest: their characteristics, age and formation. *Journal of the Geological Society* **163**: 383–399.
- Bayona G, Cortés M, Jaramillo C et al. 2003. *The Fusagasugá Succession: a Record of the Complex Latest Cretaceous-Paleogene Deformation Between the Magdalena Valley and Sabana de Bogotá Areas*. VIII Simposio Bolivariano de Cuencas Subandinas, Cartagena; 180–193.
- Benn DI, Owen LA, Finkel RC et al. 2006. Pleistocene lake outburst floods and fan formation along the Eastern Sierra Nevada, California: implications for the interpretation of intermontane lacustrine records. *Quaternary Science Reviews* **25**: 2729–2748.
- Berger GW. 1988. Dating Quaternary events by luminescence. In *Dating Quaternary Sediments*, Easterbrook DJ (ed.). Geological Society of America: Denver 13–50.
- Berger GW. 2010. An alternate form of probability-distribution plots for DE values. *Ancient TL* **28**: 11–21.
- Berger GW, Doran PT, Thomsen KJ. 2013. Micro-hole and multigrain quartz luminescence dating of Paleodeltas at Lake Fryxell, McMurdo Dry Valleys (Antarctica), and relevance for lake history. *Quaternary Geochronology* **18**: 119–134.
- Berger GW, Kratt C. 2008. LED laboratory lighting. *Ancient TL* **26**: 9–11.
- Blair TC. 2001. Outburst flood sedimentation on the proglacial Tuttle Canyon alluvial fan, Owens Valley, California, U.S.A. *Journal of Sedimentary Research* **71**: 657–679.
- Bronk-Ramsey C. 2001. Development of the radiocarbon calibration program OxCal. *Radiocarbon* **43**: 355–363.
- Bronk-Ramsey CB. 2008. Deposition models for chronological records. *Quaternary Science Reviews* **27**: 42–60.
- Brown ND, Rhodes EJ, Antinao JL et al. 2015. Single-grain post-IR IRSL signals of K-feldspars from alluvial fan deposits in Baja California Sur, Mexico. *Quaternary International* **362**: 132–138.
- Chen J, Dai F, Yao X. 2008. Holocene debris-flow deposits and their implications on the climate in the upper Jinsha River valley, China. *Geomorphology* **93**: 493–500.
- Colletta B, Hébrard F, Letouzey J et al. 1990. *Tectonic style and crustal structure of the Eastern Cordillera (Colombia), from a balanced cross section*. In *Petroleum and Tectonics in Mobile Belts*, Letouzey J (ed.). Technip: Paris 81–100.
- Cui P, Chen XQ, Wang YY et al. 2005. Jiangjia ravine debris flows in south-western China. In *Debris-Flow Hazards and Related Phenomena*, Jakob M, Hungr O (eds). Springer: Berlin 565–594.
- Dasgupta P. 2003. Sediment gravity flow—the conceptual problems. *Earth Science Reviews* **62**: 265–281.
- Dengo CA, Covey MC. 1993. Structure of the Eastern Cordillera of Colombia: implications for trap styles and regional tectonics. *American Association of Petroleum Geologists Bulletin* **77**: 1315–1337.
- Escobar J, Hodell DA, Brenner M et al. 2012. A ~43-ka record of paleoenvironmental change in the Central American lowlands inferred from stable isotopes of lacustrine ostracods. *Quaternary Science Reviews* **37**: 92–104.
- Galbraith RF, Green PF. 1990. Estimating the component ages in a finite mixture. *International Journal of Radiation Applications and Instrumentation. Part D. Nuclear Tracks and Radiation Measurements* **17**: 197–206.
- Galbraith RF, Roberts RG, Laslett GM et al. 1999. Optical dating of single and multiple grains of quartz from Jinmium rock shelter, northern Australia: Part I, Experimental design and statistical models. *Archaeometry* **41**: 339–364.
- García-Martínez R, López JL. 2005. Debris flows of December 1999 in Venezuela. In *Debris-Flow Hazards and Related Phenomena*, Jakob M, Hungr O (eds). Springer: Berlin 519–538.
- Glancy PA, Bell JW. 2000. Landslide-induced flooding at Ophir Creek, Washoe County, western Nevada, May 30, 1983. *USGS Professional Paper* 1617.
- Groot MHM, Hooghiemstra H, Berrio JC et al. 2013. North Andean environmental and climatic change at orbital to submillennial time-scales: Vegetation, water levels and sedimentary regimes from Lake Fúquene 130–27ka. *Review of Palaeobotany and Palynology* **197**: 186–204.
- Groot MHM, Bogota RG, Lourens LJ, et al. 2011. Ultra-high resolution pollen record from the northern Andes reveals rapid shifts in montane climates within the last two glacial cycles. *Climate of the Past* **7**: 299–316.
- Groote PM, Stuiver M, White JWC et al. 1993. Comparison of oxygen isotope records from the GISP2 and GRIP Greenland ice cores. *Nature* **366**: 552–554.
- Guthrie RH, Friele P, Allstadt K et al. 2012. The 6 August 2010 Mount Meager rock slide-debris flow, Coast Mountains, British Columbia: characteristics, dynamics, and implications for hazard and risk assessment. *Natural Hazards and Earth System Science* **12**: 1277–1294.
- Haug GH, Hughen KA, Sigman DM et al. 2001. Southward migration of the intertropical convergence zone through the Holocene. *Science* **293**: 1304–1308.
- Helmens KF. 1988. Late Pleistocene glacial sequence in the area of the high plain of Bogotá (Eastern Cordillera, Colombia). *Palaeogeography Palaeoclimatology Palaeoecology* **67**: 263–283.
- Helmens KF, Rutter NW, Kuhry P. 1997. Glacier fluctuations in the Eastern Andes of Colombia (South America) during the last 45,000 radiocarbon years. *Quaternary International* **38–39**: 39–48.
- Hemming SR. 2004. Heinrich events: massive Late Pleistocene detritus layers of the North Atlantic and their global climate imprint. *Reviews of Geophysics* **42**: RG1005.
- Hodell DA, Anselmetti FS, Ariztegui D et al. 2008. An 85-ka record of climate change in lowland Central America. *Quaternary Science Reviews* **27**: 1152–1165.
- Hooghiemstra H, Van der Hammen T. 1993. Late Quaternary vegetation history and paleoecology of Laguna Pedro Palo (sub-andean forest belt, Eastern Cordillera, Colombia). *Review of Palaeobotany and Palynology* **77**: 235–262.
- Hungr O. 2005. *Classification and terminology*. In *Debris-Flow Hazards and Related Phenomena*, Jakob M, Hungr O (eds). Springer: Berlin 9–23.
- Huntley DJ, Wintle AG. 1981. The use of alpha scintillation counting for measuring Th-230 and Pa-231 contents of ocean sediments. *Canadian Journal of Earth Sciences* **18**: 419–432.
- Jones SJ, Arzani N, Allen MB. 2014. Tectonic and climatic controls on fan systems: the Kohrud mountain belt, Central Iran. *Sedimentary Geology* **302**: 29–43.
- Keefer DK, Moseley ME, deFrance SD. 2003. A 38 000-year record of floods and debris flows in the Ilo region of southern Peru and its relation to El Niño events and great earthquakes. *Palaeogeography Palaeoclimatology Palaeoecology* **194**: 41–77.
- Korup O, Clague JJ. 2009. Natural hazards, extreme events, and mountain topography. *Quaternary Science Reviews* **28**: 977–990.
- Lang A. 2013. *Luminescence dating of alluvial fans and cones*. In *Dating Torrential Processes on Fans and Cones*, Schneuwly-Bölschweiler M, Stoffel M, Rudolf-Miklau F (eds). Springer: Dordrecht 283–295.
- Lavigne F, Suwa H. 2004. Contrasts between debris flows, hyper-concentrated flows and stream flows at a channel of Mount Semeru, East Java, Indonesia. *Geomorphology* **61**: 41–58.
- Lliboutry LA. 1975. La catastrophe de Yungay (Pérou). Proceedings of the Moscow Symposium, August 1971. *IAHS Publication* **104**: 353–363.

- Lowe DR, Williams SN, Leigh H et al. 1986. Lahars initiated by the 13 November 1985 eruption of Nevado del Ruiz, Colombia. *Nature* **324**: 51–53.
- Lugon R, Stoffel M. 2010. Rock-glacier dynamics and magnitude-frequency relations of debris flows in a high-elevation watershed: Ritigraben, Swiss Alps. *Global and Planetary Change* **73**: 202–210.
- Major JJ. 1997. Depositional processes in large-scale debris-flow experiments. *Journal of Geology* **105**: 345–366.
- Major JJ, Pierson TC, Scott KM. 2005. *Debris flows at Mount St. Helens, Washington, USA*. In Debris-Flow Hazards and Related Phenomena, Jakob M, Hungr O (eds). Springer: Berlin 685–731.
- Medialdea A, Thomsen KJ, Murray AS et al. 2014. Reliability of equivalent-dose determination and age-models in the OSL dating of historical and modern palaeoflood sediments. *Quaternary Geochronology* **22**: 11–24.
- Miall A. 1996. The Geology of Fluvial Deposits. Sedimentary Facies, Basin Analysis, and Petroleum Geology. Springer: Berlin.
- Murray AS, Thomsen KJ, Masuda N et al. 2012. Identifying well-bleached quartz using the different bleaching rates of quartz and feldspar luminescence signals. *Radiation Measurements* **47**: 688–695.
- Nott JF, Thomas MF, Price DM. 2001. Alluvial fans, landslides and Late Quaternary climatic change in the wet tropics of northeast Queensland. *Australian Journal of Earth Sciences* **48**: 875–882.
- Peterson LC, Haug GH, Hughen KA et al. 2000. Rapid changes in the hydrologic cycle of the tropical Atlantic during the Last Glacial. *Science* **290**: 1947–1951.
- Pierson TC. 2005. Hyperconcentrated flow – transitional process between water flow and debris flow. In Debris-Flow Hazards and Related Phenomena, Jakob M, Hungr O (eds). Springer: Berlin 159–202.
- Pierson TC, Costa JE. 1987. A rheologic classification of subaerial sediment-water flows. *Reviews in Engineering Geology* **7**: 1–12.
- Pierson TC, Scott KM. 1985. Downstream dilution of a lahar: transition from debris flow to hyperconcentrated streamflow. *Water Resources Research* **21**: 1511–1524.
- Prescott JR, Hutton JT. 1994. Cosmic ray contributions to dose rates for luminescence and ESR dating: large depths and long-term time variations. *Radiation Measurements* **23**: 497–500.
- Quigley MC, Sandiford M, Copper ML. 2007. Distinguishing tectonic from climatic controls on range-front sedimentation. *Basin Research* **19**: 491–505.
- Ray Y, Srivastava P. 2010. Widespread aggradation in the mountainous catchment of the Alaknanda-Ganga River System: timescales and implications to Hinterland-foreland relationships. *Quaternary Science Reviews* **29**: 2238–2260.
- RSNC (Red Sismológica Nacional del Colombia). 2014. Catálogo de sismos. [seisan.sgc.gov.co/RSNC/\[2014\]](http://seisan.sgc.gov.co/RSNC/[2014])
- Reimer PJ, Bard E, Bayliss A et al. 2013. IntCal13 and Marine13 radiocarbon age calibration curves 0–50,000 years cal BP. *Radiocarbon* **55**: 1869–1887.
- Rickenmann D. 2005. Runout prediction methods. In Debris-Flow Hazards and Related Phenomena, Jakob M, Hungr O (eds). Springer: Berlin 305–324.
- Riley SJ, DeGloria SD, Elliot R. 1999. A terrain ruggedness index that quantifies topographic heterogeneity. *Intermountain Journal of Sciences* **5**: 23–27.
- Rittenour TM. 2008. Luminescence dating of fluvial deposits: applications to geomorphic, palaeoseismic and archaeological research. *Boreas* **37**: 613–635.
- Schuster RL, Salcedo DA, Valenzuela L. 2002. Overview of catastrophic landslides of South America in the twentieth century. In Catastrophic Landslides: Effects, Occurrence, and Mechanisms, Evans SG, DeGraff JV (eds). The Geological Society of America: Boulder; 1–34.
- Scott KM. 1988. Origins, behavior, and sedimentology of lahars and lahar-runout flows in the Toutle-Cowlitz river system, Mount St. Helens, Washington. *United States Geological Survey Professional Paper* **1447-A**.
- Sohn YK, Rhee CW, Kim BC. 1999. Debris flow and hyperconcentrated flood-flow deposits in an alluvial fan, northwestern part of the Cretaceous Yongdong Basin, Central Korea. *Journal of Geology* **107**: 111–132.
- Spelz RM, Fletcher JM, Owen LA et al. 2008. Quaternary alluvial-fan development, climate and morphologic dating of fault scarps in Laguna Salada, Baja California, Mexico. *Geomorphology* **102**: 578–594.
- Srivastava P, Bhakuni SS, Luirei K et al. 2009. Morpho-sedimentary records at the Brahmaputra River exit, NE Himalaya: climate-tectonic interplay during the Late Pleistocene-Holocene. *Journal of Quaternary Science* **24**: 175–188.
- Suresh N, Bagati TN, Thakur RK et al. 2002. Optically stimulated luminescence dating of alluvial fan deposits of Pinjaur Dun, NW sub Himalaya. *Current Science* **82**: 1267–1274.
- Thomas MF, Thorp MB. 1995. Geomorphic response to rapid climatic and hydrologic change during the Late Pleistocene and early Holocene in the humid and sub-humid tropics. *Quaternary Science Reviews* **14**: 193–207.
- Thomsen KJ, Murray AS, Bøtter-Jensen L et al. 2007. Determination of burial dose in incompletely bleached fluvial samples using single grains of quartz. *Radiation Measurements* **42**: 370–379.
- Thrasher IM, Mauz B, Chiverrell RC et al. 2009. Luminescence dating of glaciofluvial deposits: a review. *Earth-Science Reviews* **97**: 133–146.
- USGS (United States Geological Survey). 2006. Shuttle radar topography mission. [glcf.umiacs.umd.edu/data/srtm/\[2009\]](http://glcf.umiacs.umd.edu/data/srtm/[2009]).
- USGS (United States Geological Survey). 2014. Earthquake archive. [earthquake.usgs.gov/earthquakes/search/\[2014\]](http://earthquake.usgs.gov/earthquakes/search/[2014]).
- Van der Hammen T. 1974. The Pleistocene changes of vegetation and climate in tropical South America. *Journal of Biogeography* **1**: 3–26.
- Van der Hammen T. 1995. La última glaciaciación en Colombia. *Análisis Geográfico* **24**: 69–89.
- Van Geel B, Van der Hammen T. 1973. Upper Quaternary vegetational and climatic sequence of the Fuquene area (Eastern Cordillera, Colombia). *Palaeogeography Palaeoclimatology Palaeoecology* **14**: 9–92.
- Velez MI, Hooghiemstra H, Metcalfe S et al. 2003. Pollen and diatom based environmental history since the Last Glacial Maximum from the Andean core Fuquene-7, Colombia. *Journal of Quaternary Science* **18**: 17–30.
- Vermeesch P. 2009. RadialPlotter: a Java application for fission track, luminescence and other radial plots. *Radiation Measurements* **44**: 409–410.
- Wang X, Auler AS, Edwards RL et al. 2004. Wet periods in northeastern Brazil over the past 210 kyr linked to distant climate anomalies. *Nature* **432**: 740–743.
- Wang X, Auler AS, Edwards RL et al. 2007. Millennial-scale precipitation changes in southern Brazil over the past 90,000 years. *Geophysical Research Letters* **34**: L23701.
- Wesnousky SG, Aranguren R, Rengifo M et al. 2012. Toward quantifying geomorphic rates of crustal displacement, landscape development, and the age of glaciation in the Venezuelan Andes. *Geomorphology* **141–142**: 99–113.
- Wu TS, Jaiswal MK, Lin YN et al. 2010. Residual luminescence in modern debris flow deposits from western Taiwan: A single grain approach. *Journal of Asian Earth Sciences* **38**: 274–282.
- Zhang J-F., Qiu W-L., Wang X-Q et al. 2010. Optical dating of a hyperconcentrated flow deposit on a Yellow River terrace in Hukou, Shaanxi, China. *Quaternary Geochronology* **5**: 194–199.